expected to be the most responsive to this extension, the $(1\bar{2}0)$ planes and thus the *a* axis should show the greatest stretching. This is consistent with the observations shown in Fig. 3.

The wide range of transition pressures reported in the literature for the bcc-hcp phase transition is attributable to the presence of anisotropic stress in the pressure cell and the orientation effect of the sample under pressure. In iron, the transition from the bcc to the hcp phase is always favored when the stress is applied in the direction parallel to the *a* axis of the bcc phase and when there is a shear movement along the $[1\bar{1}0]$ direction of bcc (Fig. 2). When a polycrystalline sample is compressed in a diamond anvil cell, it is likely that crystals with favorable orientation transform at pressure lower than crystals with unfavorable orientations. Thus one might find that the transition takes place at different "pressures."

The distortion of the phases in our experiment was observed in a nonhydrostatic condition where there were orientation effects arising from the presence of anisotropic stress. Using techniques similar to ours, Mao *et al.* (*7*) did not observe the anomalous lattice parameters that we did. We attribute this to some basic differences in procedure. Probably the most important difference is the method used to calculate the lattice parameters. Mao *et al.* used as many reflections as they could to calculate each lattice parameter. This had the effect of averaging out disparities resulting from lattice distortion. In our experiment we used only two reflections for calculating lattice parameters. Additional reflections that we might have used were either too weak or suffered from overlapping other reflections. The use of only two reflections greatly increased our chance of seeing the effect of lattice distortion. Another difference between the procedure followed by us and by Mao *et al.* is the time involved in collecting the data. We increased pressure and collected data points every few minutes. Mao *et al.* collected data at the rate of one point every few hundred hours. Our more rapid rate of pressure increase may have favored the martensitic-type of mechanism and the lattice distortion caused by epitaxial relationship between the phases.

In a compression study on iron, Jephcoat *et al.* (*17*) reported an anomalous compression reading in hcp iron. They found that the hcp phase has a very large *a* parameter and a normal *c* parameter, which results in an anomalously large molar volume for the hcp phase at 13.2 GPa where bcc and hcp phases coexisted. The *c*/*a* ratio was observed to be lower than the normal value in the initial stage of the phase transition (13 to 20 GPa) [see figure 4 in (*17*)]. The presence of this anomaly implies that the distorted phase can exist even under hydrostatic conditions. The nature of the anomaly, however, is apparently different as would be expected if the anisotropic stress is absent.

The explanation for this lies in the mechanism of volume reduction that takes place during the bcc-hcp phase transition. There is essentially no dimensional change between *d*(110) of bcc and *d*(002) of hcp phase (Table 1). Thus the *c*-axis dimension of the hcp phase experiences no stretching or compression even if it is constrained by an epitaxial relationship with the bcc phase. On the other hand, there is both decrease and increase in dimensions perpendicular to the *c* axis. There must, however, be a net decrease in dimension perpendicular to the *c* axis to account for the large volume change during the bcc-hcp phase transition. If this decrease in dimension is constrained by an epitaxial relationship between hcp and bcc phases, then the *a* axes of the newly formed hcp phase must on average be stretched compared with the dimensions they would have in the absence of the bcc phase. This effect does not depend on anisotropic stress or x-ray geometry and should be observable under completely isotropic conditions.

REFERENCES AND NOTES

1. D. Bancroft, E. L. Peterson, S. Minshall, *J. Appl. Phys.* **27**, 291 (1956).
2. J. C. Jamieson and A. W. Lawson, *ibid.* **33**, 776 (1962).
3. P. C. Johnson, B. A. Stein, R. S. Davis, *ibid.*, p. 557.
4. T. Takahashi and W. A. Bassett, *Science* **145**, 483 (1964).
5. F. P. Bundy, *J. Appl. Phys.* **36**, 616 (1965).
6. E. Huang *et al.*, in *High-Pressure Research in Mineral Physics*, M. H. Manghnani and Y. Syono, Eds. (Scientific Publishing, Tokyo, in press).
7. H. K. Mao, W. A. Bassett, T. Takahashi, *J. Appl. Phys.* **38**, 272 (1967).
8. B. Buras, J. Staun Olsen, L. Gerward, G. Will, E. Hinze, *J. Appl. Crystallogr.* **10**, 431 (1977).
9. M. D. Furnish and W. A. Bassett, *J. Geophys. Res.* **88**, 10333 (1983).
10. D. L. Heinz and R. Jeanloz, *J. Appl. Phys.* **55**, 885 (1984).
11. A. L. F. Vereshchagin *et al.*, *Dokl. Akad. Nauk. SSSR* **185**, 785 (1969).
12. P. G. Shewman, *Transformation in Metals* (McGraw-Hill, New York, 1969).
13. P. M. Giles, M. H. Longenbach, A. R. Marder, *J. Appl. Phys.* **42**, 4290 (1971).
14. J. W. Christian, *The Theory of Transformations in Metals and Alloys*, vol. 1, *Equilibrium and General Kinetic Theory* (Pergamon, Oxford, 1975).
15. A. G. Khachaturyan, *Theory of Structural Transformations in Solids* (Wiley, New York, 1983).
16. E. Huang *et al.*, *J. Geophys. Res.* **92**, 8129 (1987).
17. A. P. Jephcoat *et al.*, *ibid.* **91**, 4677 (1986).

6 July 1987; accepted 8 September 1987

In Situ X-ray Absorption Study of Surface Complexes: Selenium Oxyanions on α-FeOOH

KIM F. HAYES, A. LAWRENCE ROE, GORDON E. BROWN, JR., KEITH O. HODGSON, JAMES O. LECKIE, GEORGE A. PARKS

A novel application of x-ray absorption spectroscopy has provided structural information for ions sorbed at oxide-water interfaces. As an example, in situ extended x-ray absorption fine structure (EXAFS) measurements of adsorbed selenate and selenite ions at an α-FeOOH(goethite)–water interface have been performed; these measurements show that selenate forms a weakly bonded, outer-sphere complex and that selenite forms a strongly bonded, inner-sphere complex. The selenite ion is bonded directly to the goethite surface in a bidentate fashion with two iron atoms 3.38 angstroms from the selenium atom. Adsorbed selenate has no iron atom in the second coordination shell of selenium, which indicates retention of its hydration sphere upon sorption. This method provides direct structural information for adsorbed species at solid-liquid interfaces.

THE PARTITIONING OF IONS AT INTERFACES between solids and liquids is poorly understood at the molecular level, yet detailed structural information on surface complexes is essential for quantitative description of many interfacial processes. These processes play a fundamental role in a variety of fields, including geochemistry (ore deposition, metal extraction, and weathering), electrical engineering (ion-sensitive field effect transistors), catalysis (doping of oxide supports), oceanography (scavenging of trace metals), environmental engineering (removal of trace contaminants from industrial waste waters or ground water), and material science (corrosion control).

Most spectroscopic methods that are commonly used to probe interfaces require that the sample be dried and placed under high-vacuum conditions. For example, x-ray

K. F. Hayes and J. O. Leckie, Department of Civil Engineering, Stanford University, Stanford, CA 94305.
A. L. Roe and K. O. Hodgson, Department of Chemistry, Stanford University, Stanford, CA 94305.
G. E. Brown, Jr., and G. A. Parks, School of Earth Sciences, Stanford University, Stanford, CA 94305.

photoelectron spectroscopy or low-energy electron diffraction require such conditions and thus may not yield accurate information on the species responsible for the interfacial chemistry. In contrast, methods such as internal reflectance Fourier transform infrared or conversion electron Mössbauer spectroscopies can be used to study sorbed complexes in situ at solid-liquid interfaces in a limited number of cases (*1*). Another approach to the study of structural details of these sorbed complexes in situ is synchrotron-based x-ray absorption spectroscopy (XAS). Unlike Mössbauer spectroscopy, XAS is not restricted to a few elements or to specific solid-liquid systems; it is limited only by the x-ray attenuation of the substrate and liquid relative to the sorbed species (*2*). Unlike vibrational spectroscopy, XAS yields relatively accurate, direct measurements of average interatomic distance, coordination number, and the type of coordinating ligand for the nearest neighbors of the x-ray absorbing atom (*3*). As an example of the usefulness of XAS in the structural examination of species partitioned at a solid-liquid interface, the local structural environments of selenium oxyanions at an iron oxide–water interface have been determined.

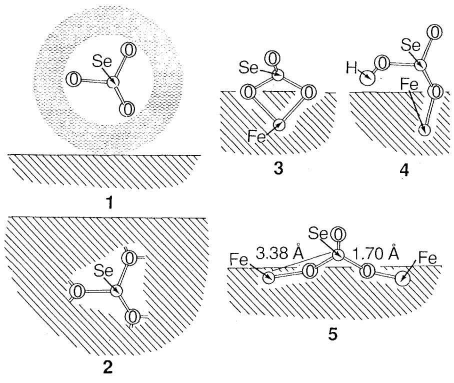

Fig. 1. Possible structures for selenite adsorbed to α-FeOOH: an outer-sphere, ion-pair adsorption complex **1** with the first hydration sphere shown as a shaded area; a solid solution of selenite **2** in the oxide phase; and inner-sphere complexes **3** through **5** on the oxide surface. Distances determined from the selenium EXAFS analysis are shown for the model structure **5**, which is consistent with the EXAFS data. The oxide is shown as the striped area below the line that represents the oxide-water interface.

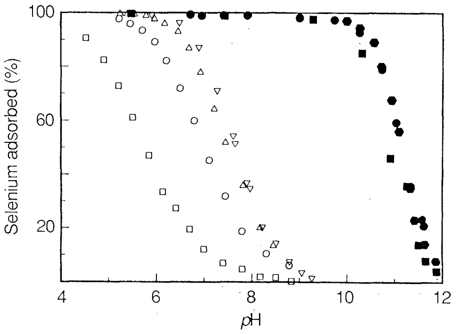

Fig. 2. Percent of the total selenium oxyanion added to solution that is adsorbed to α-FeOOH as a function of *p*H and ionic strength. The ionic strength is varied by changing the $NaNO_3$ concentration. Filled symbols represent selenite and open symbols represent selenate. Higher *p*H values and insensitivity to changes in ionic strength reflect a stronger bonding to the surface for selenite compared to selenate. The values were determined by adjusting the *p*H of a suspension of 30 g/liter α-FeOOH and 0.1 m*M* selenium oxyanion with a ^{75}Se radiotracer at the indicated ionic strength (■ and □, 1000 m*M*; ● and ○, 100 m*M*; △, 10 m*M*; •, 5 m*M*; and ▽, 1 m*M*) and then measuring the residual radioactivity of the supernatant after centrifugation.

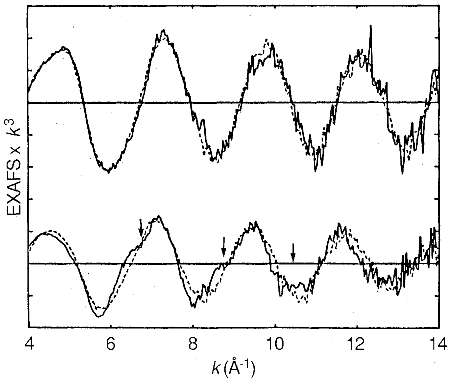

Fig. 3. EXAFS spectra of selenate (**A**) and selenite (**B**) adsorbed to α-FeOOH (solid lines) as compared with the dissolved sodium salts (25 m*M* oxyanion, *p*H = 4, dashed lines). Note that the curves are essentially identical for selenate, whereas adsorption to α-FeOOH significantly changes the EXAFS of selenite (arrows). [The EXAFS spectra are weighted by k^3 to compensate for dampening of the amplitude in the higher k value regions; this results in roughly uniform weighting of the amplitude across the entire spectrum (*11*).]

Several structural configurations for selenite and, by analogy, selenate oxyanions (SeO_3^{2-} and SeO_4^{2-}, respectively) could occur at the α-FeOOH–water interface (Fig. 1). A clear distinction can be made between inner- and outer-sphere coordination complexes of selenium at the α-FeOOH–water interface with XAS, because the presence or absence of Se-Fe second nearest neighbors can be detected and quantified by this method. We are not aware of other in situ spectroscopic methods that can provide such a conclusive description of the structure and composition of ions adsorbed at solid-liquid interfaces (*4*).

The goethite-water system was chosen because of the abundance of the mineral goethite (α-FeOOH) at the earth's surface and its important role in geochemical solid-water partitioning reactions. Selenium oxyanions were chosen as the sorbing species because selenite and selenate sorbed to goethite respond quite differently to changes in the ionic strength of the aqueous phase over a range of *p*H values (Fig. 2). The selenite ion belongs to the general class of adsorbing ions that have a strong affinity for oxide surface hydroxyl sites and whose adsorption is relatively unaffected by changes in ionic strength. The selenate ion belongs to a second class of adsorbing ions that bond weakly to such sites and whose adsorption is markedly reduced by increasing ionic strength. These ionic strength effects suggest that strongly bonded ions form inner-sphere coordination complexes with oxide surface oxygens, whereas the more weakly bonded ions form outer-sphere, ion-pair complexes that retain their primary hydration sphere upon adsorption (*5*).

To test this hypothesis, extended x-ray absorption fine structure (EXAFS) spectra were collected in fluorescence mode from an aqueous suspension of goethite (*6*) with adsorbed selenate and an identical suspension with adsorbed selenite (*7*). For comparison, the same measurements were performed in the absence of the oxide with 0.025*M* sodium selenate and selenite solutions. Spectra of sodium selenate, sodium selenite, and a cobalt selenite complex of known structure were measured in transmission mode on finely ground crystals to quantify the individual contributions to the selenium EXAFS (*8*).

The EXAFS spectra of selenium adsorbed as selenate and selenite at the α-FeOOH–water interface are compared to the spectra of their respective aqueous sodium salt solutions in Fig. 3, A and B (*7*). There is no discernible difference in the EXAFS spectra of the aqueous and adsorbed selenate samples (Fig. 3A). This suggests that there are no iron atom backscatterers at a constant bond distance within $\sim$3.5 Å of the selenium atom upon adsorption of selenate. This is consistent with selenate adsorbing as an ion-pair, outer-sphere complex with water situated between the selenate ion and the α-FeOOH surface.

The EXAFS of adsorbed selenite is significantly different from its aqueous sodium salt

Table 1. EXAFS curve-fitting parameters for selenium oxyanions in the absence and presence of α-FeOOH. Per atom amplitude and phase parameters for fitting were obtained from crystalline $MgSeO_3 \cdot 6H_2O$, Na_2SeO_4, and $[Co(NH_3)_5OSeO_2]ClO_4 \cdot H_2O$, for Se(IV)–O, Se(VI)–O, and Se(IV)–Fe, respectively (*8*). The goodness of fit is indicated by the minimization function value *F* (*9*). Based on curve-fitting analysis of the EXAFS of model compounds of known crystallographic structure, the errors in *CN* and *R* are expected to be ±20% and ±0.02 Å, respectively (*11*).

Selenium species	*CN*	*R* (Å)	$\Delta\sigma^2$†	*F*
		First shell of oxygen atoms		
SeO_3^{2-} (25 m*M*)	2.68	1.69	−0.002	0.24
SeO_3^{2-}/α-FeOOH	2.82	1.70	−0.001	0.28
SeO_4^{2-} (25 m*M*)	4.10	1.65	−0.001	0.30
SeO_4^{2-}/α-FeOOH	4.04	1.65	−0.000	0.48
SeO_3^{2-}/α-FeOOH*	2.83	1.70	−0.001	0.47
		Second shell of iron atoms		
SeO_3^{2-}/α-FeOOH*	2.10	3.38	≡0	

*Fit to the backtransform of the Fourier transform from 0.9 $Å^{-1}$ to 3.2 $Å^{-1}$. †The term $\Delta\sigma^2$ is defined in (*8*).

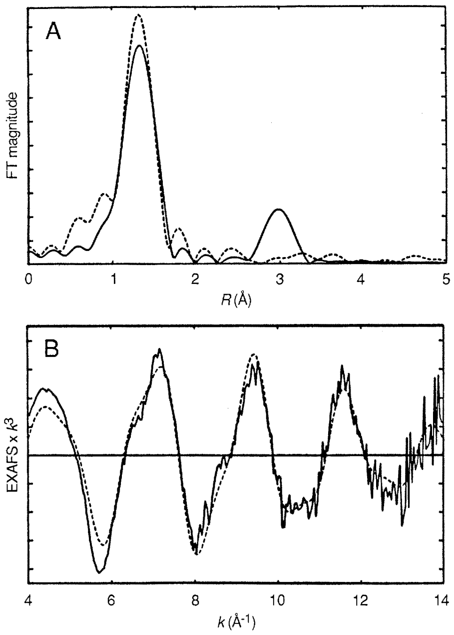

Fig. 4. (**A**) Fourier transforms of the EXAFS spectra (uncorrected for phase shifts) of selenite adsorbed to α-FeOOH (solid lines) and of selenite in solution (dashed lines). The peak in the Fourier transform of adsorbed selenite EXAFS spectrum at 2.90 Å is caused by two neighboring iron atoms at 3.38 Å from the selenium atom as determined by the curve-fitting analysis. (**B**) The best two-shell fit (dashed line) of the Fourier-filtered data of adsorbed selenite shown in (A) overlaid on the EXAFS spectrum of adsorbed selenite (solid line). (The Fourier-filtered data are backtransformed from the entire region from 0.9 Å to 3.2 Å; Table 1 gives the results of the best two-shell fit.)

solution spectrum and shows a higher frequency beat pattern that appears as shoulders (at 6.5 $Å^{-1}$, 8.7 $Å^{-1}$, and 10.3 $Å^{-1}$) to the first-shell sinusoidal oscillations (Fig. 3B). This difference is highlighted by the appearance of a second shell at 2.90 Å in the Fourier transform, which indicates the proximity of additional atoms in the coordination sphere when selenite is adsorbed (Fig. 4) (*9*). Curve-fitting analysis of the EXAFS of adsorbed selenite shows that the peak at 2.90 Å in the Fourier transform arises from two iron atoms at an average distance of 3.38 Å (Table 1 and Fig. 4B). Based on the first-shell Se–O distance of 1.70 Å, an Fe–O distance for α-FeOOH of 1.95 Å, and the Se–Fe distance of 3.38 Å, the Se–O–Fe angle is 134°. All but one of the complexes shown in Fig. 1 can be eliminated with these data: **1** would show no iron contributions to the EXAFS, **2** would have a contribution from iron two to three times greater than that observed because of a larger number of iron second nearest neighbors, and **4** would have half of the observed iron contributions; **3** would require a shorter Se–Fe distance (3.1 Å) and a smaller Se–O–Fe angle than was obtained from the EXAFS analysis. Only the selenite–α-FeOOH complex **5** is consistent with all these values, that is, an inner-sphere surface complex with the selenium atom directly coordinated to two surface oxygen atoms, which are in turn bonded to two distinct iron atoms.

The results clarify the interpretation of the effects of ionic strength on adsorption behavior, that is, that weakly bonded ions like selenate form ion-pair, outer-sphere surface complexes, whereas the more strongly bonding ions like selenite form inner-sphere surface complexes. This methodology for determining the structure and composition of adsorbed species will allow the testing of alternative models of the adsorption process (*10*). Such models are necessary to evaluate the relative importance of interfacial electrical and chemical properties and to estimate surface properties such as charge, potential, acidity, and bonding affinity (*5*).

REFERENCES AND NOTES

1. M. I. Tejedor-Tejedor and M. A. Anderson, *Langmuir* **2**, 203 (1986); F. Ambe, S. Ambe, T. Okada, H. Sekizawa, *ACS Symp. Ser.* **323**, 403 (1986).
2. In spite of its directness, the fluorescent-yield EXAFS method is not without limitations. For example, the choice of adsorbate-adsorbent system is limited by the x-ray absorption characteristics of the element of interest. In the case of selenium ions at the α-FeOOH–water interface, the Se Kα x-rays have sufficiently high energy to eliminate significant absorption from α-FeOOH or water. Other systems may not be as suitable. Another limitation is that of concentration. For the selenium systems studied, the lower concentration limit is ~1 m*M*.
3. Several excellent review articles have been written on EXAFS [see, for example, T. M. Hayes and J. B. Boyce, *Solid State Phys.* **37**, 173 (1982)].
4. Other EXAFS-based methods such as ReflEXAFS [J. Mimault *et al.*, *Springer Proc. Phys.* **2**, 479 (1984); L. Bosio, R. Cortes, G. Folcher, *J. Phys. (Paris)* **C8**, 113 (1986)] offer the potential for these types of measurements but are presently restricted to higher coverage systems.
5. K. F. Hayes and J. O. Leckie, *Colloid Interface Sci.* **115**, 564 (1987); K. F. Hayes, thesis, Stanford University (1987).
6. The α-FeOOH was synthesized by the method of R. J. Atkinson, A. M. Posner, J. P. Quirk, *Inorg. Nucl. Chem.* **34**, 2201 (1972). The resulting solid powder had a surface area of 52 m^2/g and an x-ray diffraction pattern that matched the ASTM–Joint Committee for Powder Diffraction Standards database pattern. Scanning electron microscopic examination of the particles showed them to be submicron acicular crystals of nearly uniform size, ~0.05 by 0.5 μm. All suspensions contained 30 g/liter of α-FeOOH in deionized water; the *p*H values and ionic strengths were adjusted with HNO_3, NaOH, and $NaNO_3$. Equilibrium adsorption and XAS experiments were conducted at room temperature (~22° ± 1°C). All partition and XAS measurements were performed on samples that were equilibrated for at least 24 hours but not more than 72 hours. Selenite adsorption was investigated at two coverages: 2 m*M* adsorbed (~10% surface coverage) at *p*H = 5.6 and 5 m*M* adsorbed (~25% surface coverage) at *p*H = 2.5. The analysis of the spectra for the two different coverages gave the same structural results. Only the 5 m*M* system is reported here. Selenate adsorption was investigated at only one coverage: 2 m*M* adsorbed (~10% surface coverage) at *p*H = 3.5. In all of the systems investigated, the amount of selenium adsorbed from solution was nearly 100%. The total surface site concentration was estimated to be ~20 m*M* by assuming a site density of seven sites per square nanometer.
7. The EXAFS data were collected at the Stanford Synchrotron Radiation Laboratory on beam lines IV-1 and IV-2. All suspensions and solutions were held in Teflon cells with Mylar windows. The radiation was monochromatized with Si (220) crystals and Se Kα fluorescence x-rays were measured with an ionization chamber (filled with argon) positioned at 90° to the incident radiation behind an arsenic filter [E. A. Stern and S. M. Heald, *Rev. Sci. Instrum.* **50**, 1579 (1979); F. W. Lytle *et al.*, *Nucl. Instrum. Methods Phys. Res.* **226**, 542 (1984)]. The model compounds listed in (*8*) were measured in transmission mode.
8. The EXAFS spectra of three compounds whose structures have been determined by x-ray crystallography {$MgSeO_3 \cdot 6H_2O$, P. R. Weiss, J.-P. Wendling, D. Grandjean, *Acta Crystallogr.* **20**, 563 (1966); $(NH_4)_2SeO_4$, R. L. Carter, C. Koerntgen, T. N. Margulis, *ibid.* **B33**, 592 (1977); $[Co(NH_3)_5OSeO_2](ClO_4) \cdot H_2O$, R. C. Elder and P. E. Ellis, Jr., *Inorg. Chem.* **17**, 870 (1978)} were parameterized according to:

$$\chi(k) = \sum_i (CN_i/kR_i^2)[c_0 \exp(c_2k^2)k^{c_3}] \times \sin(2kR_i + a_0 + a_1k + a_2k^2)$$

where the summation is over all sets of neighboring atoms at a distance *R*. The coordination number for the set is denoted *CN*, and $k = [2m_e(E - E_0)]^{1/2}/\hbar$, where m_e is the mass of the electron, $2\pi\hbar$ is Planck's constant, and *E* is the energy of incident x-ray beam. E_0 values of 12,666 eV and 12,670 eV were used for selenite and selenate, respectively, which were defined relative to the first inflection point of the K-edge of elemental selenium (12,654.5 eV). The term $\Delta\sigma^2$ (shown in Table 1) is the difference between the value of the EXAFS Debye-Waller factor, σ^2 (equal to $-c_2/2$), of any given sample and the value for the model compound. Further details of the analysis methods are given by S. P. Cramer, K. O. Hodgson,

E. I. Stiefel, W. E. Newton, *J. Am. Chem. Soc.* **100**, 2748 (1978). The cobalt compound was used as a model for Se-Fe EXAFS. Since the phase and amplitude parameters for Co-Se do not differ significantly from Se-Fe parameters, cobalt model compounds of similar oxidation state can be used in place of iron model compounds for the analysis (*11*). No well-characterized Fe-Se model compounds were available for this study.

9. Briefly, the important points of an EXAFS analysis are as follows. For selenium, the x-ray absorption coefficient increases sharply at 12,655 eV. This is caused by the absorption of x-ray energy and the transition of a core electron from the selenium 1*s* orbital to higher energy valence and continuum states (K-edge). Fine structure above the K-edge results from the interference between outgoing photoelectron waves (from electrons ejected to continuum states) and backscattered waves from neighboring atoms. When EXAFS data are converted to momentum space **k**, the fine structure is directly related to the sum of sinusoidal oscillations for each shell of neighboring atoms. The frequency of each oscillation is $[2kR_{\mathrm{Se-X}} + \phi(\mathbf{k})_{\mathrm{Se-X}}]$, where $R_{\mathrm{Se-X}}$ is the bond length between selenium and neighboring atom X and $\phi(\mathbf{k})_{\mathrm{Se-X}}$ is the phase function specific to selenium and atom X (since the frequency is directly related to the bond length, the EXAFS contribution from an iron atom at twice the distance of the first shell of oxygen atoms will have a frequency twice that of the EXAFS contribution of the first shell). After the $\phi(\mathbf{k})$ values have been determined from "model" compounds of known structure, the bond lengths and coordination number for a given shell can be determined by a least-squares fit of a theoretically calculated curve to the experimental EXAFS data. The measure of the goodness of fit is given by the minimization function value F, defined as $F = \{\Sigma[k^3(\chi_{\mathrm{obs}} - \chi_{\mathrm{calc}})^2]/n\}^{1/2}$, where χ_{obs} and χ_{calc} are the observed and calculated EXAFS, respectively, and n is the number of data points.
10. G. Sposito, *ACS Symp. Ser.* **323**, 217 (1986).
11. B. K. Teo and P. A. Lee, *J. Am. Chem. Soc.* **101**, 2815 (1979).

12. We gratefully acknowledge the support of the Environmental Protection Agency (EPA R-809561) and the National Science Foundation (CHE 8512129 and EAR 8513488). The Stanford Synchrotron Radiation Laboratory is supported by the U.S. Department of Energy and the Biotechnology Resource Program of the National Institutes of Health.

29 June 1987; accepted 22 September 1987

New Routes to Early Memories

DAVID KUCHARSKI* AND W. G. HALL

Stimulation of one side of the olfactory system during training with odor-milk pairings in neonatal rats results in their ability to recall an odor memory by using the trained but not the untrained side of the brain. In 12-day-old rats, olfactory learning can be recalled by stimulation of either the trained or untrained side. The development of bilateral recall reflects the maturation of olfactory commissural pathways that provide access to the olfactory memory stored on the contralateral side. Furthermore, the commissural pathways need not be present at the time of memory formation but can establish new and specific access to already existing olfactory memories.

NORMALLY, THE RIGHT AND LEFT sides of the brain are in communication through a series of commissures, fiber systems that cross the midline to form reciprocal connections between corresponding bilateral structures. Sectioning the major commissure, the corpus callosum, causes animals to behave in many situations as if they have two separate brains (*1*). With hemispheres disconnected, for example, each half of the brain can exhibit relatively independent perception, learning, and memory when the inflow of sensory information is restricted to one side. We have recently shown that newborn rats behave as a "natural split-brain preparation" in an olfactory learning protocol (*2*). Specifically, in rats younger than 12 days of age, the memory for a learned odor is confined to one side of the brain if a single naris is stimulated during pairings of an odor and milk reward. Such pups show increased preference for the odor in a choice task when tested with the same naris that was open during training; they show no such preference when tested with the other naris open. In contrast, when pups 12 days of age or older are trained unilaterally, they show learned preference with either naris open. This bilateral response develops simultaneously with the maturation of specific components of the anterior commissure (*3*), the olfactory system's crossed projection pathway. Indeed, the anterior commissure pathways are crucial for bilateral olfactory learning in older pups because cutting them before training restores unilateral conditioning (*2, 4*). However, even in older pups showing bilateral preference, the olfactory memories are still stored unilaterally, as demonstrated by a unilateral preference when the commissure is sectioned after training.

Although these findings indicate that commissural fibers can provide access to unilateral olfactory memories and confirm that the functional maturation of these pathways occurs between 6 and 12 days after birth, they raise an additional question. Do the newly formed crossed connections gain access to already formed memories, previously inaccessible to one side of the brain, or does bilateral access require existence of connections at the time of learning? To study this question we examined the recall of unilateral learning in 12-day-old rat pups that had been trained at 6 days of age. Unilateral training thus occurred in the absence of commissural projections to target layers in the contralateral anterior olfactory nucleus and piriform cortex (*3*). Pups were then tested at 12 days, when projections providing bilateral access had developed. To ensure that any bilateral access observed was the result of new access to memories (and not, for example, a duplication of learning on the untrained side), we sectioned the anterior commissure in some pups to confirm unilateral storage of the olfactory preference memories.

Forty-eight 6-day-old pups (*5*) received ten training trials consisting of a 20-second exposure to cedar odor, provided to one naris, starting 15 seconds before and continuing during the brief 5-second infusion of milk (*6, 7*). Cedar-milk pairings occurred every minute for 10 minutes. Milk rewards were delivered through small cannulas installed in pups' mouths (*7, 8*). We confined odor to one naris by inserting a soft rubber plug into the opposite nostril (*9*). After the conditioning, the nose plug was switched to the other naris for half of the pups and was sham-switched (removed and reinserted into the same naris) for the other half. Half an hour after pups had received the training treatment, they were tested for their response to cedar odor in a two-choice preference test (*10*) in which they were allowed to spend time over cedar-scented or unscented shavings. The number of seconds spent over

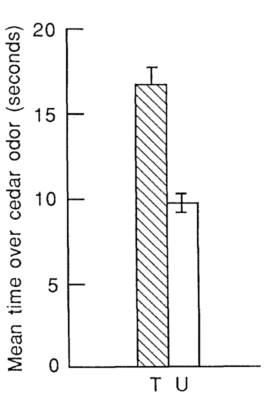

Fig. 1. Mean number of seconds over cedar during each preference test (maximal score, 30 seconds) as a function of naris open during the preference test administered at 6 days of age. T, trained naris; U, untrained naris. Error bars represent SEM. This finding of unilateral olfactory learning at 6 days of age replicates the results of our previous studies (*2*).

Department of Psychology, Duke University, Durham, NC 27706.

*On 24 October 1987, Dr. Kucharski died in an automobile accident.